Journal of Magnetic Resonance 251 (2015) 26–35

Contents lists available at ScienceDirect

Journal of Magnetic Resonance

journal homepage: www.elsevier.com/locate/jmr

High resolution *in-operando* microimaging of solar cells with pulsed electrically-detected magnetic resonance

Itai Katz [a], Matthias Fehr [b], Alexander Schnegg [b], Klaus Lips [b,*], Aharon Blank [a,*]

[a] Schulich Faculty of Chemistry, Technion – Israel Institute of Technology, Haifa 32000, Israel
[b] Helmholtz-Zentrum Berlin für Materialien und Energie, Institut für Silizium-Photovoltaik and Berlin Joint EPR Laboratory (BeJEL), Kekuléstr. 5, D-12489 Berlin, Germany

ARTICLE INFO

Article history:
Received 1 September 2014
Revised 13 November 2014
Available online 9 December 2014

Keywords:
ESR
EPR
Electrically-detected magnetic resonance
Semiconductor defects

ABSTRACT

The *in-operando* detection and high resolution spatial imaging of paramagnetic defects, impurities, and states becomes increasingly important for understanding loss mechanisms in solid-state electronic devices. Electron spin resonance (ESR), commonly employed for observing these species, cannot meet this challenge since it suffers from limited sensitivity and spatial resolution. An alternative and much more sensitive method, called electrically-detected magnetic resonance (EDMR), detects the species through their magnetic fingerprint, which can be traced in the device's electrical current. However, until now it could not obtain high resolution images in operating electronic devices. In this work, the first spatially-resolved electrically-detected magnetic resonance images (EDMRI) of paramagnetic states in an operating real-world electronic device are provided. The presented method is based on a novel microwave pulse sequence allowing for the coherent electrical detection of spin echoes in combination with powerful pulsed magnetic-field gradients. The applicability of the method is demonstrated on a device-grade 1-μm-thick amorphous silicon (a-Si:H) solar cell and an identical device that was degraded locally by an electron beam. The degraded areas with increased concentrations of paramagnetic defects lead to a local increase in recombination that is mapped by EDMRI with ~20-μm-scale pixel resolution. The novel approach presented here can be widely used in the nondestructive *in-operando* three-dimensional characterization of solid-state electronic devices with a resolution potential of less than 100 nm.

1. Introduction

Paramagnetic species are an inseparable and essential part of any solid-state device, from the simplest diode through solar cells, complex three-dimensional silicon-based chips, and up to futuristic quantum computing devices. Many paramagnetic species are intentionally inserted into the material (e.g., neutral phosphorus in silicon) while others represent unwanted by-products, such as point defects and crystal impurities. Thus, both desirable and undesirable paramagnetic species constitute an inevitable part of the electronic devices' functionality [1–3]. Traditionally, the identification, study, and manipulation of such paramagnetic entities are carried out using electron spin resonance (ESR). For example, in the case of point defects, impurities, or states induced by local disorder in inorganic and organic semiconductors, ESR makes it possible to characterize the defects' atomic structure [4–8], learn about impurity concentrations and distributions [9,10], and bridge the gap between paramagnetic and electronic properties [11,12]. However, the limited sensitivity of ESR often allows neither *in-operando* studies of real-world devices nor mapping the paramagnetic manifold on a nanoscale level.

One approach recently adopted in order to resolve these problems involves the development of an ultra-high-sensitivity ESR imaging setup that makes use of miniature microwave resonators [13,14] coupled with high-performance gradient coils [15]. For an isotopic-enriched phosphorous-doped ^{28}Si sample (^{28}Si:P) it was shown that a sensitivity of less than 1000 electron spins of the neutral P atom and a spatial resolution of less than 1 μm can be achieved [16]. While this represents a significant milestone in the field of ESR spectroscopy, it should be mentioned that this performance can only be achieved on samples with long spin lattice (T_1) and spin–spin (T_2) relaxation times. While some important devices may be based on such materials [17,18], most real-world samples are much more challenging.

A different approach to the ultra-sensitive detection of paramagnetic species in solid-state samples is based on electrical

* Corresponding authors at: Institute Silicon Photovoltaics, Helmholtz-Zentrum Berlin für Materialien und Energie, Kekuléstr. 7, 12489 Berlin, Germany. Tel.: +49 30 8062 14960; fax: +49 30 8062 15074 (K. Lips). Tel.: +972 4 829 3679; fax: +972 4 829 5948 (A. Blank).
E-mail addresses: lips@helmholtz-berlin.de (K. Lips), ab359@tx.technion.ac.il (A. Blank).

http://dx.doi.org/10.1016/j.jmr.2014.11.008
1090-7807/

detection, which was introduced in the 1970s and is known today as electrically-detected magnetic resonance (EDMR) [19]. EDMR monitors spin-dependent current changes and is selective to electronic transitions between paramagnetic states that contribute to charge carrier transport. By combining the spectroscopic information contents of ESR with the sensitivity of a charge current measurement, EDMR provides a perfect *in-operando* tool to study the impact of paramagnetic states on the electric device's performance with an almost single spin detection limit [20–22]. There are several possible mechanisms that can result in spin-dependence of the charge carrier current, e.g., hopping, trapping, recombination, and tunneling through paramagnetic states. If these electronic processes involve localized states, the spin-dependent mechanism is usually associated with the formation of spin pairs [23]. Under steady state conditions, a certain occupation of the possible spin-pair configuration (four in case of two spin 1/2 particles) will emerge, which may then be disturbed by a resonant microwave irradiation. This will lead to changes in the occupation and hence to transitions between the different spin-pair configurations that can be detected as a net change in the charge carrier current. The charge transport routes gated in this manner by magnetic resonance spin manipulations may be those associated with device efficiency, such as leakage currents, recombination through defect states, or hopping through localized states in photovoltaic devices [24], or they may exist as part of the desired device attributes, e.g., in organic electronic and spintronic devices [25], depending on the type of the device and experimental conditions (applied voltage, temperature, etc.) [26–28]. In the EDMR detection scheme, the energy quanta to be detected per spin is in the order of eV, depending on the device's operating voltage, which is ~4–5 orders of magnitude larger than the energy quanta per spin in a typical ESR induction detection scheme. This leads to a much improved spin sensitivity of about 100 spins or better in a broad range of materials and devices [21,29], thus dramatically surpassing the conventional spin sensitivity attainable via the conventional method known as induction detection.

The EDMR method can be employed either with continuous microwave irradiation (CW-EDMR) or with pulsed microwave excitation (pulsed EDMR – pEDMR). The former is simpler [19], while the latter is more complicated [30] but offers considerably more information about the relaxation properties of the paramagnetic species involved and the mechanism and dynamics of the spin-dependent process. With EDMR, the magnetic fingerprint of the spin species involved in charge carrier transport can be easily collected to allow a full *in-operando* analysis of the material or the device [8].

In recent years, pEDMR has developed into a mature technique and has incorporated the most common pulsed ESR detection sequences, e.g., rotary echoes [31,32], Hahn-echo sequences [33,34], electron spin echo envelope modulation (ESEEM) [35,36], electron–electron double resonance (ELDOR) [37], and electron nuclear double resonance (ENDOR) detection [38,39]. However, a major drawback of the EDMR technique is that it spatially integrates over the conductive area of the sample under study, and therefore provides no spatial resolution unless multiple contacts are used and little current spreading exists.

A recent method that potentially provides both spectral and spatial high resolution images is the EDMR microscope based on a combined ESR-AFM setup with a conductive tip [40]. This method succeeded in providing measurable EDMR signals with sufficient *g*-factor resolution and a spatial resolution determined by the size of the $\sim 3 \times 3\ \mu m^2$ electrode. However, this EDMR microscope suffers from significant current noise due to the instability of the AFM contact. Furthermore, it requires the performance of sequential scanning of the surface, and its current sensing mechanism is not necessarily local due to current spreading and also cannot be generalized to three-dimensional (3D) imaging requirements. A major difference between the CW-EDMR microscope and the method presented here is that the latter relies on coherent spin manipulation.

Another alternative to enhance the spatial resolution of EDMR, suggested more than a decade ago, involves the use of fixed magnetic field gradients which spatially encode the sample in conjunction with CW-EDMR data acquisition [41]. This approach is relatively simple technically-wise but very ineffective when the sample has a broad spectral line width, leading to a very crude spatial separation. The first experimental proof was accomplished on a crystalline silicon wafer, on which an image resolution of ~1.9 mm was obtained using gradients of ~0.2 T/m [41]. Clearly, such limited resolution is of no practical use to the vast majority of materials and electronic devices of relevance; consequently, this approach was not developed further.

In this paper we present a novel approach that makes use of a new pEDMR detection protocol combined with powerful pulsed magnetic-field gradients to provide EDMR images of the paramagnetic states in operating thin-film silicon solar cells with an experimental spatial resolution of ~20 μm. Furthermore, since the resolution in our experiment is limited mostly by the current noise, with an optimized sample layout a resolution of ~100 nm could be within reach. The new EDMR imaging scheme retains the complete ESR information regarding the paramagnetic spectrum of the measured species, thereby enabling their spatially-resolved assignment and *in-operando* characterization. Therefore, our line of work is very promising and can lead to a new type of ESR analysis tool for solid-state electronic devices with both high spatial and spectroscopic resolution.

2. Materials and methods

EDMR measurements were carried out on thin-film silicon solar cells (see Fig. 1) with 1-μm-thick hydrogenated amorphous silicon (a-Si:H) absorber layers sandwiched between microcrystalline silicon (μc-Si) p and n layers, and transparent top and bottom contacts made from Al-doped ZnO. Solar cell samples were deposited on quartz substrates by plasma-enhanced chemical vapor deposition in superstrate configuration [42], which allows illumination through the substrate.

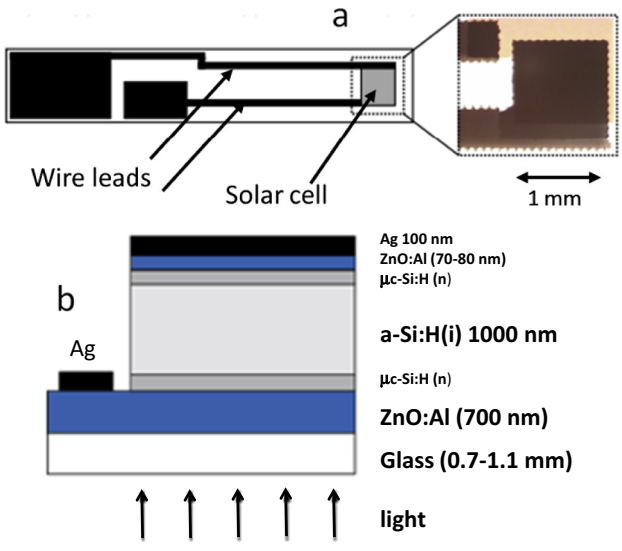

Fig. 1. (a) General layout of the a-Si:H thin-film silicon solar cell used in this study. A close-up of the solar cell is shown on the right. (b) Lateral structure of the cell; light enters through the glass substrate.

In order to modulate the spatial distribution of dangling bond defects using high energy electrons [43,44], some of the solar cells were exposed to the 20-KeV electron beam (e-beam) of a scanning electron microscope through the top contact opposite to the substrate (top layer in Fig. 1b). An electron current of ~13.5 nA and a dose of 10 mC/cm^2 was applied at a beam energy of 20 KeV to engrave a diamond-shaped pattern of 500 × 500 μm^2 into the cell, thereby increasing the spatially inhomogeneous defect concentration. Throughout the manuscript we refer to e-beam-treated samples as e-beam-degraded solar cells, whereas the untreated samples are called "as-deposited" solar cells.

3. The pulsed EDMR microimaging setup

First, let us briefly describe the principles of pEDMR and then show how it can be generalized to include imaging capabilities. The most basic pEDMR detection scheme is shown in Fig. 2a [30]. In pEDMR the observable is a transient current, ΔI, induced following intense microwave (MW) pulses. In solar cells the pEDMR signals may have positive or negative signs, depending on the underlying transport process and operating conditions (see for example [28] for an overview on spin-dependent transport processes in solar cells).

Another possible sequence used in pEDMR is the electrically-detected electron spin echo (ED-ESE), which is an extension of the standard two-pulse Hahn echo sequence with an additional $\pi/2$ readout pulse at the time of echo formation (see Fig. 2b) [33]. The last MW pulse rotates the spin system back into singlet or triplet states, thereby transferring electron coherence to polarization. The echo amplitude is obtained using time-integration of ΔI after the third MW pulse. To strobe the whole spin echo, the pulse sequence has to be iterated for varying τ_2 times (however, for imaging purposes, acquiring a single echo point is enough). In addition, as we discuss below, the imaging scheme we employ requires having the full complex information about the spins' magnetization [45], i.e., both the I (in-phase) and Q (out-of-phase) components of the magnetization as it precesses in the XY laboratory plane (with the Z-axis along the static magnetic field). In order to obtain these quantities we introduce here a new scheme where this ED-ESE sequence is repeated twice, the first time with the detection pulse with X phase and then with Y phase. The first type of detection pulse flips to the Z-axis only the MW-affected spins that were positioned prior to the pulse along the Y-axis, while the second type of detection pulse flips to the Z-axis the magnetization that was positioned along the $-X$ axis. The combination of these two measurements provides the full complex data about the spins precessing in the XY-plane at the time of the echo.

Now, let us see how this detection scheme can be generalized to include imaging capabilities. Generally speaking, to obtain an ESR image, magnetic field gradients have to be applied to spatially encode the signal coming from the sample [46]. As noted above, a fixed magnetic field gradient combined with CW-EDMR detection is of no practical use, mainly due to the wide inhomogenously-broadened spectral line of most relevant samples. On the other hand, previous research on EDMR with a variety of samples has clearly shown that it is a coherent phenomenon whose exhibited behavior includes Rabi oscillations and echo refocusing [34]. These characteristics can in principle be exploited to obtain high resolution ESR images making use of pEDMR detection combined with so-called pulsed phase gradients for spatial encoding [45,47]. In this imaging method, spatial information is encoded in the ESE phase angles by transient magnetic field gradients, as sketched in Fig. 2c and d for the temporal and spatial domains, respectively. Gradients are applied during the first delay (τ_1) of the ESE sequence. The gradient strength (G_0, G_1, ...) is incremented

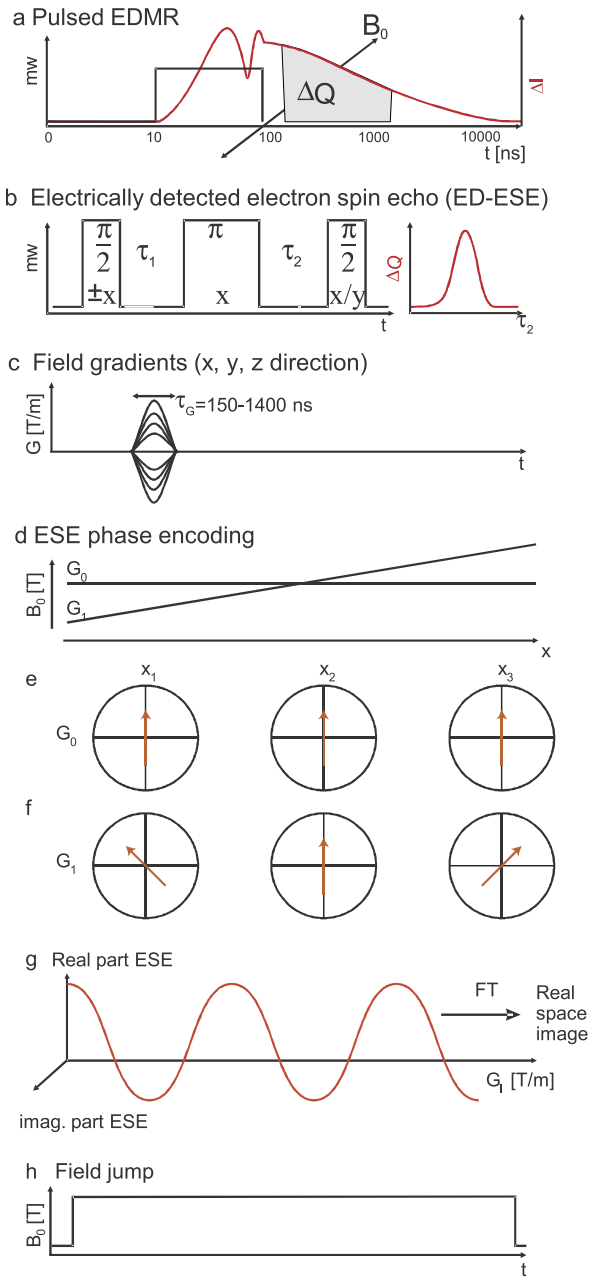

Fig. 2. (a) Basic field-swept simple one-pulse pEDMR sequence. (b) ED-ESE MW sequence with the ED-ESE plotted vs. τ_2. $\pm X$ and X/Y indicate the MW phases of the first and third pulse, respectively. (c) Timing of the transient magnetic field gradients relative to the MW pulses. (d) Spatial magnetic field offset with (G_1) and without (G_0) field gradient. (e) and (f) circles indicating rotating frames of reference (one-dimensional example) for electron spins (red arrows) located at three different points in space (x_1, x_2 and x_3) without and with applied field gradient, respectively. (g) Oscillating ESE intensity vs. field gradient. In the case shown here for three spin "points" symmetric about the origin, the imaginary part of the phase encoded echo is exactly canceled out. However, in the more general arbitrary spin distribution, this would not be the case: some of the echo signal might also be in the imaginary part, and thus both its I and Q components need to be adequately sampled. (h) Timing of the magnetic field jump that switches between on- and off-EDMR conditions. (For interpretation of the references to color in this figure legend, the reader is referred to the web version of this article.)

step-wise and for each step the ESE amplitude and phase is recorded. To illustrate the phase gradient imaging principle, their impact on electron spins located at three different points in space (x_1, x_2, x_3, respectively) is shown in Fig. 2e and f with respect to circles indicating rotating frames of reference (one-dimensional

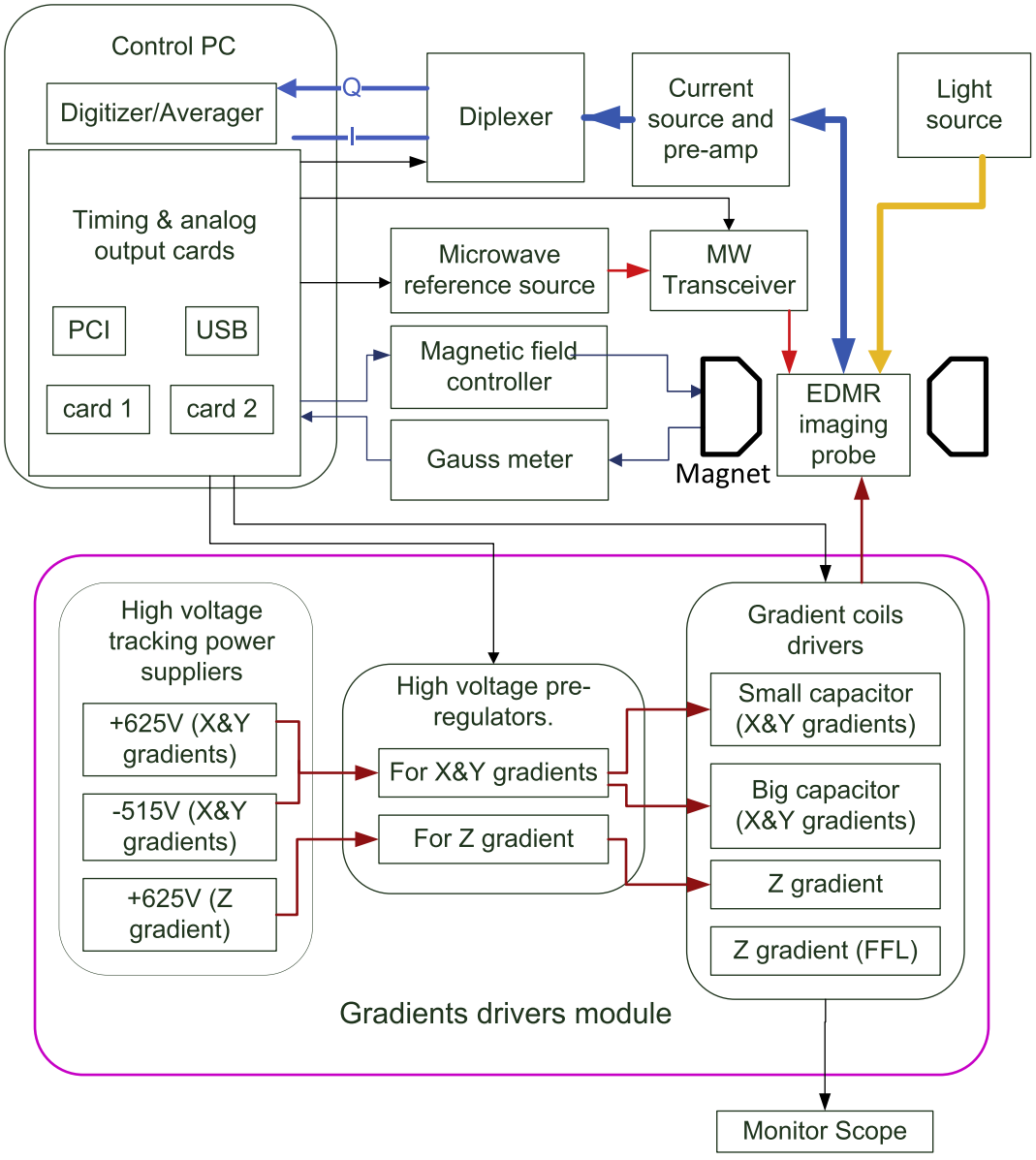

Fig. 3. Schematic block diagram of the pulsed EDMR imaging system (see also description in Ref. [49]). A computer (control PC) triggers MW pulses in the MW transceiver. These pulses go into the EDMR imaging probe, which is also fed by magnetic-field gradient pulses to spatially encode the sample, and by continuous light excitation to create charge carries at cryogenic temperatures in the solar cell. The current in the solar cell is measured by a home-made differential current preamplifier and then goes into a diplexer (by mini-circuits) that feeds either the "*I*" or "*Q*" inputs of the digitizing card, depending on the phase of the third pulse in the imaging sequence (see also main text).

example). If no magnetic field gradient is applied (G_0), all three electron spins remain stationary in the rotating frame (Fig. 2e). In the case of a finite gradient (G_i), electron spin j acquires a phase angle $\varphi_{ij} = \gamma x_j \int_{\tau_c} G_i dt$, which results in I and Q components of the ESE intensity of $I \sim \sum_j \cos(\varphi_{ij})$ and $Q \sim \sum_j \sin(\varphi_{ij})$ (Fig. 2f). Thus, in the general case, as a result of the phase gradients the ESE intensity and phase will oscillate as a function of G_i. As depicted in Fig 2g, a Fourier transform (FT) of this oscillating signal with respect to G_i yields the real space distribution of the electron spins.

The practical realization of such imaging scheme requires overcoming some major experimental issues of concern. For example, pEDMR makes use of very sensitive current measurements of the sample under test. However, the MW pulses, especially the magnetic field gradient pulses, create large transient currents along the wire leads. To cancel this disturbance, we implemented a two-stage solution that includes both MW phase cycling and the application of a "field jump" protocol. Phase cycling is based on a ± phase modulation of the first MW pulse in the sequence (see Fig. 2b) [48], which in turn modulates the phase of the echo signal. By repeating the sequence once with the $+X$ phase and then with the $-X$ phase, and then subtracting the results, the current transient is eliminated while the coherent EDMR echo signal that follows the phase of the first pulse is reinforced. The "field jump" protocol provides yet another mechanism for the reduction of the current transient (see Fig. 2h). Here again, the current measurement is repeated twice, once "on resonance" and then "off resonance", by applying a fast current pulse through an auxiliary coil in the imaging probe that quickly (within a few microseconds) changes the resonance field. The unwanted current artifacts are the same under both conditions and can thereby be eliminated by subtracting "off resonance" from "on resonance" current transients. Thus, by applying this two-stage solution (phase cycling and field jump), spin-dependent and spin-independent electrical responses may be separated from each other.

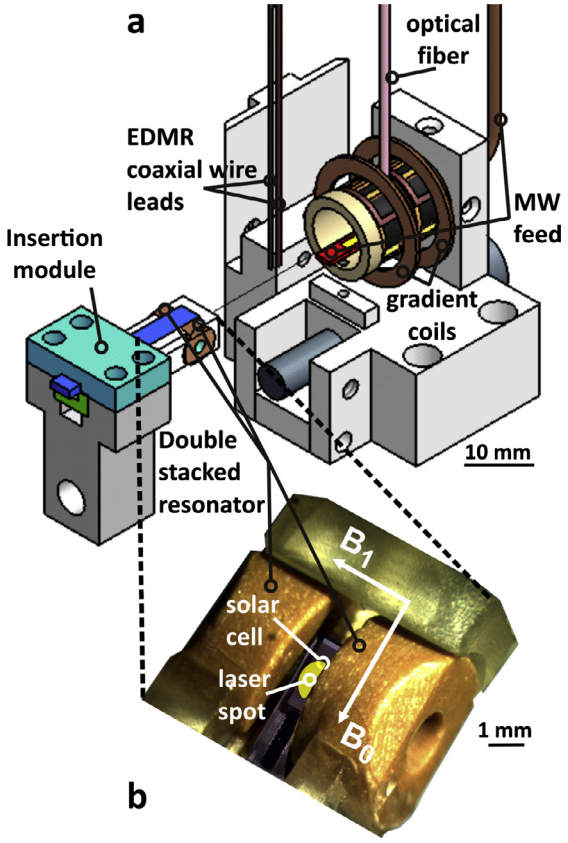

Fig. 4. (a) Drawing of the cryogenic pEDMRI probe with electrical and optical supply lines, the gradient coil array, and the resonator insertion module with mounted solar cell. (b) A close-up photograph indicating the position of the solar cell inside the double-stacked resonator (ring dimensions: o.d. = 4.4 mm, i.d. = 1.5 mm, height = 2.3 mm, distance from pair ring = 1.4 mm). The directions of the external static magnetic field (B_0), the magnetic field component of the microwave (B_1), and the illumination (when inserted into the gradient coils) are overlaid on the image.

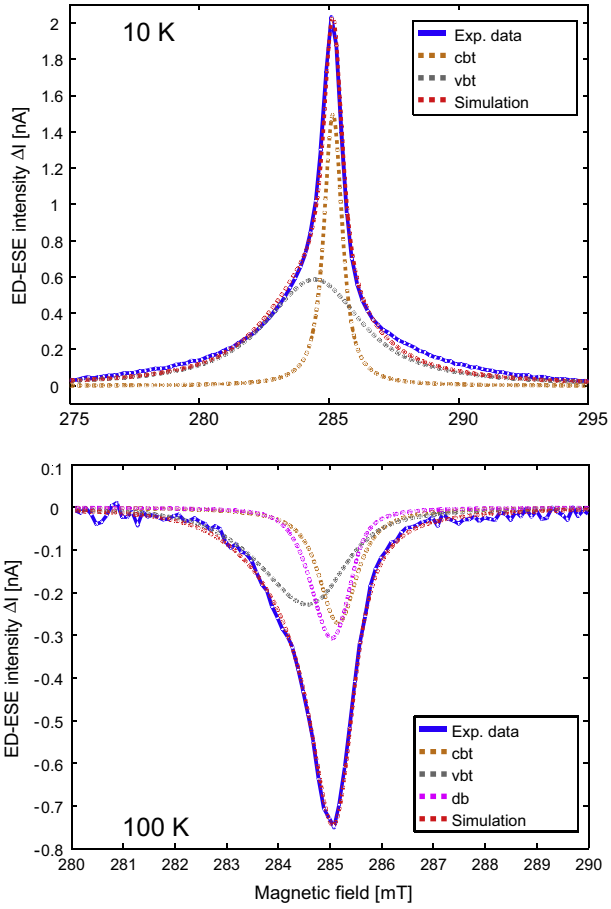

Fig. 5. ED-ESE spectra of an irradiated a-Si:H solar cell at 10 K (top) and 100 K (bottom), respectively. Absolute ED-ESE intensities were obtained with the three-pulse MW sequence described in Fig. 2b. Together with the experimental spectra (blue solid lines), spectral simulations (red dashed lines) assuming contributions from conduction band tail (CBT) states (green dashed lines), valance band tail (VBT) states (grey dashed lines), and dangling bond states (DBs) (pink dashed lines) are plotted, with their respective g values provided in the legend. Experimental parameters: MW frequency = 8.3 GHz, light intensity = ~0.2 suns (200 W/m^2), $\tau_1 = \tau_2 = 400$ ns, current was sampled 100 ns after the third pulse in the sequence with sampling window of 200 ns, MW pulse lengths were $\pi/2 = 70$ and $\pi = 130$ ns (spectral resolution of ~0.25 mT), bias voltage over the cell = −0.74 V, DC current under illumination = 80 μA and 0.9 μA at 100 K and 10 K, respectively, accumulations per field point = 50,000, and repetition rate = 20 kHz. (For interpretation of the references to color in this figure legend, the reader is referred to the web version of this article.)

The novel pulsed EDMR imaging setup that was developed in this work is schematically described in Fig. 3. The measurement setup is based on our conventional pulsed ESR microimaging system's architecture [49] together with our cryogenic pulsed ESR probe head [15], adapted to operate at 8.3 GHz. In order to facilitate the generation and acquisition of the pulse sequence described in Fig. 2, we had to implement some software and hardware modifications in the system and in the cryogenic probe head, respectively. Fig. 4 depicts a drawing of the cryogenic pEDMRI probe together with a close-up photograph of the resonator and the mounted solar cell. We used a dielectric resonator based on a double-stacked ring structure made of DR80 material from TCI Ceramics, Inc. The quality factor of the resonator is ~50, as measured by a vector network analyzer. For EDMR detection, we extended the cryogenic probe (see Fig. 4) with an optical fiber in order to illuminate the solar cell using a halogen lamp or, alternatively, a green laser; we also added two shielded coaxial electrical leads to supply the solar cell with a voltage bias and to measure the photocurrent. Microwaves are supplied via a coaxial MW feed line that goes into the gradient coil fixture, where it is turned into a microstrip line through an appropriate adapter. The microstrip line then goes below the resonator structure and excites the double-stacked resonator by capacitive coupling. The line position can be varied with respect to the resonator by *XY*-stages to match the resonator's apparent impedance to that of the transmission line. In this position the solar cell is also connected to the coaxial wire leads and can be illuminated by the optical fiber.

With respect to the detection system shown in Fig. 3, we added a sensitive current preamplifier for EDMR detection [50]. Furthermore, in order to sample properly the in-phase and out-of-phase components of the magnetization, we made use of a computer-controlled diplexer switch (Mini-Circuits' model ZYSW-2-50DR) that directs the EDMR signal to the appropriate channel (I or Q) of the analog digitizer card in the computer. In principle, the I and Q signals can be sampled with a single digitizing channel, at different time windows. However, in the present case we preferred to employ a hardware-based diplexer solution for sampling the I and Q signals in order to minimize the need for significant software modification with respect to our conventional induction–detection ESR imaging setup. In addition, we implemented a software upgrade that properly controls EDMR spectroscopy and imaging sequences. This novel setup provides now the unique possibility of performing coherent pEDMR spectroscopy and imaging on fully processed (real-world) electronic devices with unmatched spatial resolution.

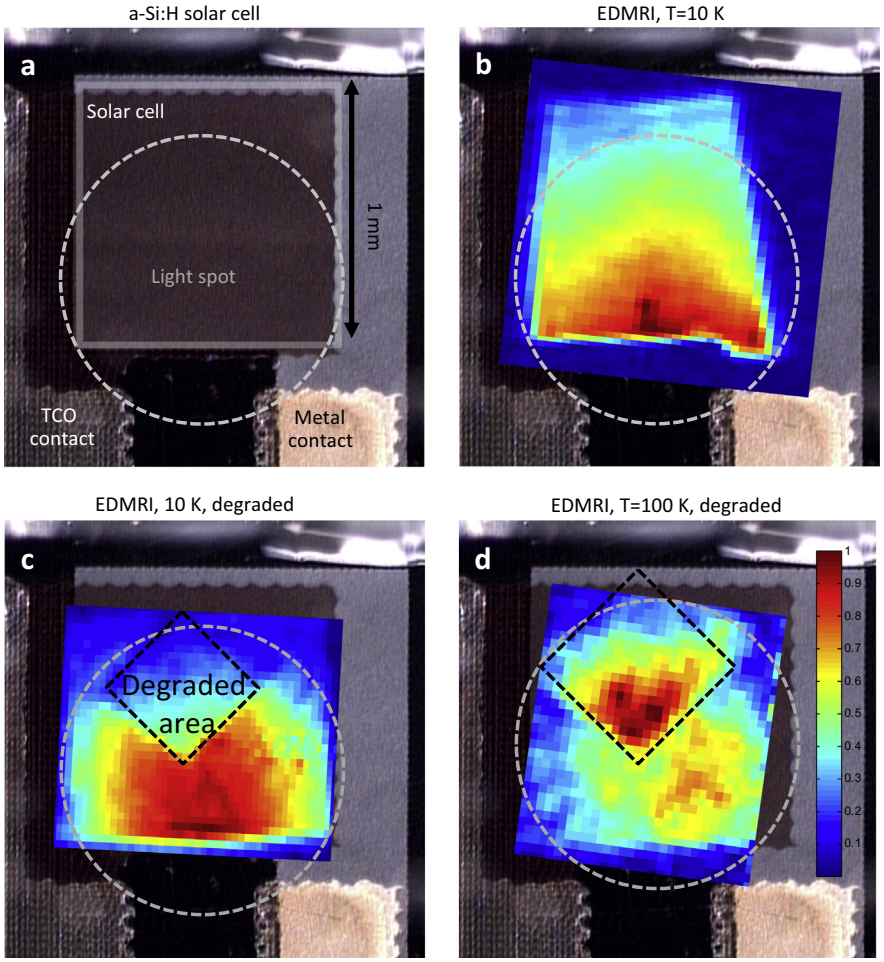

Fig. 6. (a) Photo of the solar cell and its components, showing also the illumination area. (b) pEDMR image of the illuminated as-deposited solar cell at 10 K, when measured inside the double-stacked dielectric resonator. (c) and (d) pEDMR images of the e-beam-degraded solar cell, measured at 10 and 100 K, respectively. The degraded area is framed by the dashed diamond shape. The color code appearing in (d) is linearly scaled and normalized to the largest pixel signal in each image. Experimental parameters: MW frequency = 8.3 GHz, light intensity = ~0.2 suns (200 W/m^2), $\tau_1 = \tau_2 = 500$ ns, current was integrated from the time range of 100–8000 ns after the third pulse of the sequence, MW pulse lengths were $\pi/2 = 60$ and $\pi = 120$ ns, magnetic field gradients $\tau_G = 400$ ns, maximum strength $G = 6.5$ T/m (for the X axis) and $G = 4.3$ T/m (for the Y axis), bias voltage over the cell = −0.74 V, DC current under illumination = 70 μA and 0.8 μA at 100 K and 10 K, respectively, and repetition rate = 20 kHz and 4 kHz, respectively.

4. Results and discussions

Before embarking on the actual EDMR microimaging experiments, we performed conventional pEDMR measurements to identify dominating noise sources that limit the detection sensitivity of the EDMRI spectrometer, and to measure the spin coherence time.

Fig. 5 presents field-swept ED-ESE spectra recorded on an illuminated hydrogenated amorphous silicon (a-Si:H) pin solar cell, following selective e-beam irradiation on its central part (see Section 2), at 100 K and 10 K. The e-beam irradiation causes the generation of dangling bonds and enhances recombination losses in the solar cell [43,44]. Spectra were recorded with the echo sequence depicted in Fig. 2b, without applying a field gradient or field jump. From the data depicted in Fig. 5 we obtained relative EDMR-induced current changes (relative to the DC photocurrent of the cell) of $\Delta I/I \sim 9.25 \times 10^{-6}$ and $\Delta I/I \sim 0.0022$ at 100 K and 10 K, respectively. The single-shot noise RMS level was ~9 nA (100 K) and 4.5 nA (10 K). This is roughly ~4 and 15 times higher than the predicted shot-noise level (assuming a detection bandwidth of 200 kHz). In the 100-K measurement, this is probably due to noise contributions from the device itself and instabilities in the intensity of the halogen light source. In the 10-K measurement, the solar cell current shows less noise and the light source instability may be identified as the dominant noise source. In both cases, thermal noise is not significant. The single-shot signal-to-noise ratios were 0.087 (100 K) and 0.43 (10 K).

The proper setting of the imaging pulse sequence requires prior knowledge about phase memory times, T_m. By varying the pulse separation time τ_1 from 0.5 μs to 4 μs we were able to estimate the EDMR-detected T_m as ~3.6 μs, which was found to be the same at 10 K and 100 K. This T_m is long enough to fit in the phase gradients between the 90° and 180° MW pulses, without excessive loss of echo signal.

In order to better understand the sign of the current transient shown in Fig. 5 and to assign spin-dependent charge transport processes in the solar cell, we carried out the detailed spectroscopic analysis that is provided in Appendix A. Our conclusion from this analysis is that at 10 K, the pEDMR signal is due to hopping processes among conduction and valance band tail states [51,52], while at 100 K, the main contribution to the EDMR signal is due to recombination by Si dangling bonds.

On the basis of the parameters obtained from ED-ESE spectroscopy, we proceeded to perform two-dimensional pEDMRI on as-deposited and e-beam-degraded a-Si:H solar cells. Fig. 6a shows a photograph of the a-Si:H solar cell together with the illumination profile. Fig 6b shows the pEDMR image of the as-deposited solar cell measured at 10 K under illumination overlaid on the photograph of the solar cell. For pEDMRI we chose the same MW pulse

parameters as for ED-ESE spectroscopy. In addition, we applied 400-ns-long magnetic field gradients and the field jump protocol, outlined in Fig. 2c and d. With these parameters and an accumulation time of ~4 h, pEDMR images (100 × 64 pixels) were obtained. The pEDMR image depicted in Fig 6b is somewhat distorted due to non-uniform gradient magnitudes (which in principle can be corrected by off-line image analysis). Nevertheless, the pixel resolution of ~22 × 34 μm clearly resolves the boundaries of the solar cell and the modulation of spin-dependent transport over the cell. This modulation is due to the excitation profile of the light source, which in our current setup does not illuminate the solar cell uniformly. The spatial distribution of the spin-dependent transport signal over the cell may be rationalized by the underlying processes. First, higher light intensity results in a larger photocurrent and therefore a larger overall measured ΔI. Second, at 10 K and with an applied bias, the pEDMR signal is dominated by spin-dependent hopping via conduction band tail (CBT) and valence band tail (VBT) states. With increasing light intensity, the quasi-Fermi level of holes and electrons is pushed closer to the edges of the conduction and valence band, and hence into regions with a higher density of states. This results in a decrease in average hop times, which enhances the EDMR signal's intensity, $\Delta I/I$.

Subsequently, we carried out pEDMRI on a solar cell that was subjected to e-beam degradation within a 500 μm × 500 μm diamond-shaped region (see Section 2). Fig. 6c and d depict pEDMR images obtained from the irradiated cell at 10 K and 100 K, respectively. Except for the number of pixels (64 × 40 at 100 K and 80 × 60 at 10 K), these images were acquired with the same experimental parameters as Fig. 6b.

When comparing 10-K pEDMR images obtained on as-deposited (Fig. 6b) and e-beam-degraded (Fig. 6c) solar cells, spin-dependent current patterns may be identified. In both cases, the strength of the spin-dependent hopping signal depends on the excitation profile of the light source. However, the e-beam-degraded cell shows also a pronounced decrease of the spin-dependent current as compared to the as-deposited cell. This interesting finding is not fully understood yet. Possible reasons could be an increase of non-spin-dependent recombination pathways via doubly-occupied dangling bonds [52], or a reduction of the average hop time due to the shift of the a-Si:H quasi-Fermi levels towards midgap where defects can be generated by the e-beam exposure [53].

Upon increasing the temperature, the pEDMR image of the solar cell changes again dramatically (see Fig. 6d). At 100 K, the e-beam-irradiated region exhibits a strongly increased EDMR signal as compared to the surrounding parts of the solar cell. This is in agreement with many observations showing that e-beam-irradiation increases the number of dangling bonds and leads to increased spin-dependent trapping and recombination (revealed here through local spatially-resolved data). This also supports the EDMR spectroscopy data in Appendix A which showed that the 100-K EDMR signal originates from recombination involving CBT states and DBs. This reduction of the lifetime is manifested in an increase in EDMR signal intensity.

These first high resolution functional *in-operando* pEDMR images on real-world solar cells demonstrate the potential of this novel technique to locate spin-dependent transport and loss mechanisms in an electronic device, and reveal the spatial distribution of function-determining paramagnetic states in fully processed electronic devices.

5. Conclusions and future prospects

The basic approach to pulsed EDMR imaging by pulsed phase gradients has proven to work well. Nevertheless, there is still plenty of room for improvement. The fundamental limiting factor in our pEDMR imaging experiment is the signal-to-noise ratio (SNR). Our phase gradient drivers can provide much more powerful gradients than the ones used in this experiment, and currently support resolutions down to 80 nm [49,54]. However, at such resolution the noise level in our experiment will be too high, since the number of defects, or states, in a given voxel will be too small to observe. Improvements in SNR can be achieved, first of all, by using a more stable light source that does not have significant noise components at the ~1–500 kHz range. This can increase SNR by a factor of ~4 by reaching the shot-noise limit. Furthermore, increasing the light intensity to at least 3.2 suns would lead to ~16 times more current than obtained here, meaning an increase in SNR by a factor of 4. Additional significant improvements can be gained by using smaller cells with a smaller overall shot noise (e.g., a cell with a size of ~10 × 10 μm would lead to a hundredfold improvement in SNR).

The cumulative effect of these near-future improvements can increase SNR by a factor of ~1600, meaning that it is possible to reach an image resolution in the scale of a few hundreds of nanometers for the type of cells we employed here. We can estimate the concentration of the defect states that contribute to the spin-dependent current component in this material to be $\sim 10^{16}$ states per cm^3 [55]. This means that Fig. 6b shows $\sim 10^7$ states in each voxel in the EDMR image, with an SNR of ~200. Clearly, it would not have been possible to obtain such sensitivity (and consequently, image resolution) with such sample and spin properties using conventional ESR. Other solar cells or semiconductor devices that have paramagnetic species or states with larger concentrations may make it possible to reach even higher spatial resolutions in the nanometer scale. For example, since an EDMR signal for P-doped Si can be obtained for less than 100 spins, it follows that a 3D resolution of ~100 nm should be readily available with such type of sample having a P concentration of $\sim 10^{16}$ atoms/cm^3.

The method developed here can be widely used for the nondestructive inspection of paramagnetic species in a variety of solid-state electronic devices, especially in the emerging field of nanostructured or nanocomposite 3D semiconductor devices. Although the experimental results presented here have limited resolution, relatively simple future improvements will greatly enhance the capabilities of the pulsed EDMRI experiment, resulting in resolutions on the scale of hundreds of nanometers. It should also be noted that our setup can support also 3D and 4D imaging capabilities (with the 4th dimension referring to the EDMR spectrum).

It is worth mentioning that the presented EDMRI technique has a potential for defect characterization on electronic devices that goes beyond imaging of spin-dependent electronic transport, by providing images of the *total current of the device*. Many devices would normally have a homogenous spin-dependent EDMR current signature, meaning that $\Delta I/I$ should be the same for the entire device. However, EDMR imaging of such devices may still reveal some significant heterogeneity, which in such cases may result only from local changes in the overall current. The latter which may be quenched or enhanced in the device due to defects unrelated to spins or spin-dependent processes, such as crystal dislocations.

Acknowledgments

This work was partially supported by Grant #G-1032-18.14/2009 from the German–Israeli Foundation (GIF), Grant #213/09 from the Israeli Science Foundation, Grants #201665 and #309649 from the European Research Council (ERC), and by the Russell Berrie Nanotechnology Institute at the Technion. MF received funding from the German Research Foundation within SPP 1601. We thank F. Finger and O, Astakhov (Forschungszentrum

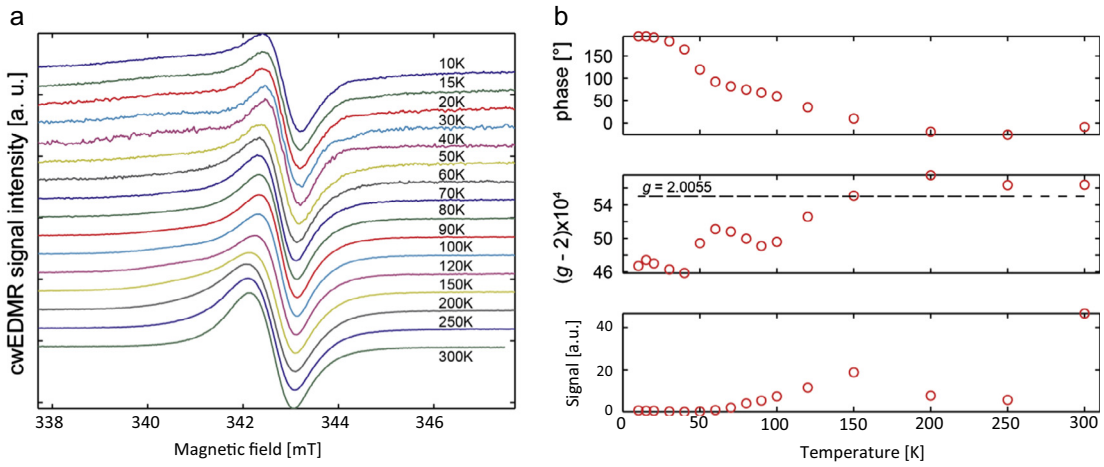

Fig. A1. (a) Normalized CW-EDMR spectra of an irradiated solar cell as a function of temperature, showing real part. The magnetic field has been rescaled to the same MW frequency. (b) CW-EDMR phase, g value, and signal amplitude corresponding to data shown in (a). Measurement conditions: $U = 0$ V, illumination with halogen lamp (1 sun at the sample), X-Band Bruker Elexsys (ER-4118X MD5 resonator), MW frequency = 9.5 GHz, MW power = 10 dB, modulation amplitude = 0.4 mT, modulation frequency = 10 kHz. The error in phase determination is ±5°.

Jülich) for supplying the solar cells that were prepared through the BMBF-funded network project EPR-Solar (03SF0328).

Appendix A. Spectroscopic analysis of the EDMR signal at various temperatures

The source of the spin-dependent current (the EDMR signal) can be different at various temperatures. These processes can be mainly revealed through spectroscopic analysis of the EDMR signal (g factors). Additional supporting evidence can be obtained by looking at alternations in the sign of the pEDMR current. For example, it is clear that the spectra shown in Fig. 5 differ with respect to their sign, resonance position, and line shape. These differences originate in the fact that different spin-dependent transport processes dominate in a-Si:H at different temperatures [52,53,56]. The current enhancing signal (positive current change) measured at 10 K can be interpreted through its spectroscopic signature as a superposition of a narrow resonance at $g = 2.004$ and a broad line at $g = 2.010$. This pEDMR spectrum can be assigned to two independent spin-dependent hopping processes among conduction band tail states (CBT, $g = 2.0044$ [51]) and valence band tail states (VBT, $g = 2.01$ [51,52]), respectively. Upon increasing the temperature to 100 K, the sign of the spin-dependent current reverses and the main contribution to the spectrum is shifted to $g = 2.005$. The resulting EDMR spectra can be interpreted as originating from spin-dependent tunneling of trapped CBT electrons into neutral Si dangling bonds (DB, $g = 2.0055$ [6,52]). A subsequent hole capture completes this recombination loss mechanism. At 100 K, this signal still contains some contribution from VBT states; this disappears above 200 K (see below), as has been previously reported for a-Si:H films [52].

The assignment of spin-dependent transport processes was further corroborated by X-band CW and pulsed EDMR measurements performed under varying ambient conditions. The CW-EDMR measurements of the sample after e-beam degradation are shown in Fig. A1a. The measurements were performed under short-circuit conditions ($U = 0$ V) and under light illumination. All spectra underwent post-processing to adjust the phase so as to minimize the quadrature (out-of phase) signal. The phase rotation angle which was applied to the individual spectra is plotted in A1b. A strong CW-EDMR signal could be observed at room temperature with a value of $g = 2.0056$. At lower temperatures, a signal with a value of $g = 2.0046$ was observed with a phase value larger by 203° than the CW-EDMR spectrum observed at room temperature. The phase shift and the observed g value supports the evidence that the signals at room temperature and low temperature originate from different mechanisms. As we argue above, at room

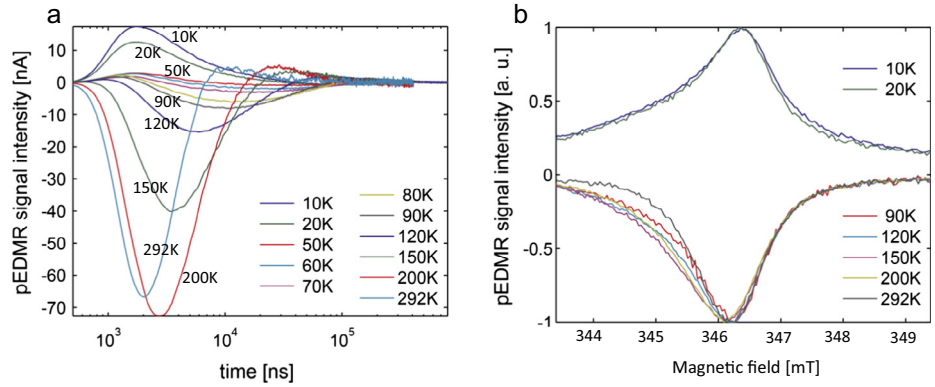

Fig. A2. Pulse EDMR transients (a) of an irradiated solar cell and normalized spectra (b) as a function of temperature. Measurement conditions: $U = 0$ V, illumination with Halogen lamp (1 sun at the sample), X-Band Bruker Elexsys (ER-4118X MD5 resonator), MW frequency = 9.5 GHz, MW power = 18 dB, pulse length = 120 ns. Current was samples 100 ns after the MW pulse with acquisition windows of 200 ns. Number of accumulations was 10,000 for each time trace.

temperature the EDMR signal is probably due to a spin-dependent recombination through dangling bond defects, while the low-temperature signal is probably due to spin-dependent hopping among conduction band tail states. In addition to these measurements, pulsed EDMR experiments were performed to provide an additional perspective regarding the manner in which different spin-dependent transport processes dominate at different temperatures. The transient EDMR signal after a 120-ns microwave π pulse was measured. The results are shown in Fig. A2, where Fig. A2a displays the transient signal at the maximum of the spectrum and Fig. A2b shows the spectrum at a time t after the pulse, where the transient signal has reached a maximum (for a current enhancing signal) or minimum (for a current quenching signal). One advantage of pulsed EDMR over the CW-EDMR experiment is that changes in the sign of the spin-dependent current can be observed more easily without phase ambiguity, which sometimes is harder to control in CW measurements. Fig. A2 clearly shows that the signal at low temperatures (10–50 K) has a different sign than at higher temperatures. In these measurements, the polarity of the current detection setup was chosen so that the total photocurrent flowing through the solar cell is positive; therefore, we believe that the positive signal of Fig. A2 corresponds to an absolute current-enhancing signal. If that is so, this supports further the indications that spin-dependent hopping among conduction band tail states is the dominant EDMR mechanism observed at these temperatures. Additional support comes from the measured value for $g = 2.004$, which is identical to the g value of conduction band tail states in a-Si:H [51,52]. At higher temperatures (90–292 K), the sign of the spin-dependent current changes and a strong negative transient EDMR signal is observed, supporting the claim that under these conditions a spin-dependent recombination through dangling bond defects is observed. This is further corroborated by the value $g = 2.0055$, which is identical to the g value of dangling bond defects [6,52]. At intermediate temperatures it is difficult to distinguish clearly between hopping and recombination, because the transient EDMR signal becomes small and has both positive and negative contributions. Results from ED-ESE spectroscopy may also be correlated with the pEDMRI images recorded at 10 K and 100 K to complete the picture of these spin-dependent mechanisms operating at different temperatures.

References

[1] G.D. Watkins, EPR of defects in semiconductors: past, present, future, Phys. Solid State 41 (1999) 746–750.
[2] R. Jansen, Silicon spintronics, Nat. Mater. 11 (2012) 400–408.
[3] B.E. Kane, A silicon-based nuclear spin quantum computer, Nature 393 (1998) 133–137.
[4] G. Feher, Electron spin resonance experiments on donors in silicon. I. Electronic structure of donors by the electron nuclear double resonance technique, Phys. Rev. 114 (1959) 1219.
[5] M. Stutzmann, D.K. Biegelsen, R.A. Street, Detailed investigation of doping in hydrogenated amorphous-silicon and germanium, Phys. Rev. B 35 (1987) 5666–5701.
[6] M. Fehr, A. Schnegg, B. Rech, K. Lips, O. Astakhov, F. Finger, G. Pfanner, C. Freysoldt, J. Neugebauer, R. Bittl, C. Teutloff, Combined multifrequency EPR and DFT study of dangling bonds in a-Si:H, Phys. Rev. B 84 (2011) 245203.
[7] N.S. Sariciftci, L. Smilowitz, A.J. Heeger, F. Wudl, Photoinduced electron-transfer from a conducting polymer to buckminsterfullerene, Science 258 (1992) 1474–1476.
[8] B.M. George, J. Behrends, A. Schnegg, T.F. Schulze, M. Fehr, L. Korte, B. Rech, K. Lips, M. Rohrmuller, E. Rauls, W.G. Schmidt, U. Gerstmann, Atomic structure of interface states in silicon heterojunction solar cells, Phys. Rev. Lett. 110 (2013) 136803.
[9] A.M. Tyryshkin, S.A. Lyon, A.V. Astashkin, A.M. Raitsimring, Electron spin relaxation times of phosphorus donors in silicon, Phys. Rev. B 68 (2003) 193207.
[10] A.M. Tyryshkin, S. Tojo, J.J.L. Morton, H. Riemann, N.V. Abrosimov, P. Becker, H.J. Pohl, T. Schenkel, M.L.W. Thewalt, K.M. Itoh, S.A. Lyon, Electron spin coherence exceeding seconds in high-purity silicon, Nat. Mater. 11 (2012) 143–147.
[11] A.A. Istratov, H. Hieslmair, E.R. Weber, Iron and its complexes in silicon, Appl. Phys. A-Mater. 69 (1999) 13–44.
[12] M. Warner, S. Mauthoor, S. Felton, W. Wu, J.A. Gardener, S. Din, D. Klose, G.W. Morley, A.M. Stoneham, A.J. Fisher, G. Aeppli, C.W.M. Kay, S. Heutz, Spin-based diagnostic of nanostructure in copper phthalocyanine-C-60 solar cell blends, ACS Nano 6 (2012) 10808–10815.
[13] Y. Twig, E. Dikarov, A. Blank, Ultra miniature resonators for electron spin resonance. Sensitivity analysis, design and construction methods, and potential applications, Mol. Phys. 111 (2013) 2674–2682.
[14] R. Narkowicz, D. Suter, I. Niemeyer, Scaling of sensitivity and efficiency in planar microresonators for electron spin resonance, Rev. Sci. Instrum. 79 (2008) 084702.
[15] Y. Twig, E. Dikarov, A. Blank, Cryogenic electron spin resonance microimaging probe, J. Magn. Reson. 218 (2012) 22–29.
[16] A. Blank, E. Dikarov, R. Shklyar, Y. Twig, Induction-detection electron spin resonance with sensitivity of 1000 spins: en route to scalable quantum computations, Phys. Lett. A 377 (2013) 1937–1942.
[17] J.J.L. Morton, D.R. McCamey, M.A. Eriksson, S.A. Lyon, Embracing the quantum limit in silicon computing, Nature 479 (2011) 345–353.
[18] A. Blank, Scheme for a spin-based quantum computer employing induction detection and imaging, Quantum Inf. Process. 12 (2013) 2993–3006.
[19] D.J. Lepine, Spin-dependent recombination on silicon surface, Phys. Rev. B 6 (1972) 436.
[20] M. Xiao, I. Martin, E. Yablonovitch, H.W. Jiang, Electrical detection of the spin resonance of a single electron in a silicon field-effect transistor, Nature 430 (2004) 435–439.
[21] D.R. McCamey, H. Huebl, M.S. Brandt, W.D. Hutchison, J.C. McCallum, R.G. Clark, A.R. Hamilton, Electrically detected magnetic resonance in ion-implanted Si:P nanostructures, Appl. Phys. Lett. 89 (2006) 182115.
[22] F.H.L. Koppens, K.C. Nowack, L.M.K. Vandersypen, Spin echo of a single electron spin in a quantum dot, Phys. Rev. Lett. 100 (2008) 236802.
[23] C. Boehme, K. Lips, Charge Transport in Disordered Solids with Applications in Electronics, Wiley, 2006, pp. 179–219.
[24] M. Fehr, P. Simon, T. Sontheimer, C. Leendertz, B. Gorka, A. Schnegg, B. Rech, K. Lips, Influence of deep defects on device performance of thin-film polycrystalline silicon solar cells, Appl. Phys. Lett. 101 (2012) 123904.
[25] D.D. Awschalom, N. Samarth, Trend: spintronics without magnetism, Physics 2 (2009) 50.
[26] D. Kaplan, I. Solomon, N.F. Mott, Explanation of large spin-dependent recombination effect in semiconductors, J. Phys. Lett-Paris 39 (1978) L51–L54.
[27] C. Boehme, K. Lips, Theory of time-domain measurement of spin-dependent recombination with pulsed electrically detected magnetic resonance, Phys. Rev. B 68 (2003) 245105.
[28] A. Schnegg, J. Behrends, M. Fehr, K. Lips, Pulsed electrically detected magnetic resonance for thin film silicon and organic solar cells, Phys. Chem. Chem. Phys. 14 (2012) 14418–14438.
[29] C. Boehme, K. Lips, The ultra-sensitive electrical detection of spin-Rabi oscillation at paramagnetic defects, Phys. B-Condens. Matter 376 (2006) 930–935.
[30] C. Boehme, K. Lips, Time domain measurement of spin-dependent recombination, Appl. Phys. Lett. 79 (2001) 4363–4365.
[31] C. Boehme, K. Lips, Electrical detection of spin coherence in silicon, Phys. Rev. Lett. 91 (2003) 246603.
[32] J. Behrends, K. Lips, C. Boehme, Observation of precursor pair formation of recombining charge carriers, Phys. Rev. B 80 (2009) 045207.
[33] H. Huebl, F. Hoehne, B. Grolik, A.R. Stegner, M. Stutzmann, M.S. Brandt, Spin echoes in the charge transport through phosphorus donors in silicon, Phys. Rev. Lett. 100 (2008) 177602.
[34] G.W. Morley, D.R. McCamey, H.A. Seipel, L.C. Brunel, J. van Tol, C. Boehme, Long-lived spin coherence in silicon with an electrical spin trap readout, Phys. Rev. Lett. 101 (2008) 207602.
[35] F. Hoehne, J.M. Lu, A.R. Stegner, M. Stutzmann, M.S. Brandt, M. Rohrmuller, W.G. Schmidt, U. Gerstmann, Electrically detected electron-spin-echo envelope modulation: a highly sensitive technique for resolving complex interface structures, Phys. Rev. Lett. 106 (2011) 196101.
[36] M. Fehr, J. Behrends, S. Haas, B. Rech, K. Lips, A. Schnegg, Electrical detection of electron-spin-echo envelope modulations in thin-film silicon solar cells, Phys. Rev. B 84 (2011) 193202.
[37] F. Hoehne, H. Huebl, B. Galler, M. Stutzmann, M.S. Brandt, Spin-dependent recombination between phosphorus donors in silicon and Si/SiO_2 interface states investigated with pulsed electrically detected electron double resonance, Phys. Rev. Lett. 104 (2010).
[38] D.R. McCamey, J. Van Tol, G.W. Morley, C. Boehme, Electronic spin storage in an electrically readable nuclear spin memory with a lifetime > 100 seconds, Science 330 (2010) 1652–1656.
[39] F. Hoehne, L. Dreher, H. Huebl, M. Stutzmann, M.S. Brandt, Electrical detection of coherent nuclear spin oscillations in phosphorus-doped silicon using pulsed ENDOR, Phys. Rev. Lett. 106 (2011) 187601.
[40] K. Klein, B. Hauer, B. Stoib, M. Trautwein, S. Matich, H. Huebl, O. Astakhov, F. Finger, R. Bittl, M. Stutzmann, M.S. Brandt, The electrically detected magnetic resonance microscope: combining conductive atomic force microscopy with electrically detected magnetic resonance, Rev. Sci. Instrum. 84 (2013) 103911.
[41] T. Sato, H. Yokoyama, H. Ohya, H. Kamada, Imaging of electrically detected magnetic resonance of a silicon wafer, J. Magn. Reson. 153 (2001) 113–116.

[42] Y. Mai, S. Klein, R. Carius, H. Stiebig, X. Geng, F. Finger, Open circuit voltage improvement of high-deposition-rate microcrystalline silicon solar cells by hot wire interface layers, Appl. Phys. Lett. 87 (2005) 073503.
[43] U. Schneider, B. Schroder, F. Finger, Saturation effect and annealing behavior of metastable defects induced by Kev – electron-irradiation in intrinsic a-Si-H, J. Non-Cryst. Solids 114 (1989) 633–635.
[44] O. Astakhov, R. Carius, F. Finger, Y. Petrusenko, V. Borysenko, D. Barankov, Relationship between defect density and charge carrier transport in amorphous and microcrystalline silicon, Phys. Rev. B 79 (2009) 104205.
[45] A. Coy, N. Kaplan, P.T. Callaghan, Three-dimensional pulsed ESR imaging, J. Magn. Reson. Ser. A 121 (1996) 201–205.
[46] P.T. Callaghan, Principles of Nuclear Magnetic Resonance Microscopy, Oxford University Press, Oxford, 1991.
[47] A. Blank, C.R. Dunnam, P.P. Borbat, J.H. Freed, Pulsed three-dimensional electron spin resonance microscopy, Appl. Phys. Lett. 85 (2004) 5430–5432.
[48] F. Hoehne, L. Dreher, J. Behrends, M. Fehr, H. Huebl, K. Lips, A. Schnegg, M. Suckert, M. Stutzmann, M.S. Brandt, Lock-in detection for pulsed electrically detected magnetic resonance, Rev. Sci. Instrum. 83 (2012) 043907.
[49] L. Shtirberg, Y. Twig, E. Dikarov, R. Halevy, M. Levit, A. Blank, High-sensitivity Q-band electron spin resonance imaging system with submicron resolution, Rev. Sci. Instrum. 82 (2011) 043708.
[50] J. Behrends, A. Schnegg, M. Fehr, A. Lambertz, S. Haas, F. Finger, B. Rech, K. Lips, Electrical detection of electron spin resonance in microcrystalline silicon pin solar cells, Philos. Mag. 89 (2009) 2655–2676.
[51] T. Umeda, S. Yamasaki, J. Isoya, K. Tanaka, Microscopic origin of light-induced ESR centers in undoped hydrogenated amorphous silicon, Phys. Rev. B 62 (2000) 15702–15710.
[52] H. Dersch, L. Schweitzer, J. Stuke, Recombination processes in a-Si-H – spin-dependent photoconductivity, Phys. Rev. B 28 (1983) 4678–4684.
[53] K. Lips, S. Schutte, W. Fuhs, Microwave-induced resonant changes in transport and recombination in hydrogenated amorphous-silicon, Philos. Mag. B 65 (1992) 945–959.
[54] L. Shtirberg, A. Blank, Short, powerful, and agile current drivers for magnetic resonance, Concept Magn. Reson. B 39B (2011) 119–127.
[55] T. Umeda, S. Yamasaki, J. Isoya, A. Matsuda, K. Tanaka, Energy location of light-induced ESR centers in undoped a-Si:H, J. Non-Cryst. Solids 227 (1998) 353–357.
[56] M.S. Brandt, M. Stutzmann, Spin-dependent conductivity in amorphous hydrogenated silicon, Phys. Rev. B 43 (1991) 5184–5187.